Force-free Simulations of Ultra-Relativistic Jets

Alexander Tchekhovskoy*, Jonathan C. McKinney† and Ramesh Narayan*

*Harvard-Smithsonian Center for Astrophysics, 60 Garden Street, Cambridge, MA 02138, USA
†Kavli Institute for Particle Astrophysics and Cosmology, Stanford University, P.O. Box 20450, MS 29, Stanford, CA 94309, USA; Chandra Fellow

Abstract. We describe time-dependent axisymmetric numerical simulations of ultrarelativistic highly-magnetized, force-free jets. The simulations follow the jet from the central engine to beyond six orders of magnitude in radius. The simulated jets are confined by an external pressure which we take to vary as a power-law with distance along the jet. We find that the radial distance over which the jet is pressure supported determines the terminal Lorentz factor. For the collapsar model of GRBs, this distance is set by the size of the progenitor star and is very large. At this distance our fiducial model generates a Lorentz factor $\gamma \sim 400$ and a half-opening angle $\theta_j \sim 2^\circ$, consistent with observations of many long GRBs. Other models with slightly different parameters give γ in the range 100 to 5000 and θ_j from 0.1° to 10°, thus reproducing the range of properties inferred for GRB jets. A potentially observable feature of some of our solutions is that both γ and the Poynting flux S are concentrated in hollow cones, with the half-opening angle of the γ-cone $\theta_\gamma \ll \theta_j$ and the half-opening angle of the S-cone $\theta_S = \theta_j$. In the case of systems such as AGN, XRBs, and short GRBs, we expect the confining medium, viz., the disk wind, to act over a shorter range of distance. This would explain the lower terminal Lorentz factor of these systems compared to long GRBs.

Keywords: plasma magnetohydrodynamics – astrophysical jets – gamma-ray bursts – black holes
PACS: 95.30.Qd; 95.30.Sf; 98.58.Fd; 98.70.Rz; 97.60.Lf; 97.60.Jd

INTRODUCTION

Models of long gamma-ray bursts (GRBs) require the ejected plasma to move at ultra-relativistic speeds [1]. For some bursts the required Lorentz factor may be as high as $\gamma \sim 400$ [2], and the jet half-opening angle may be $\theta_j \sim$ a few degrees [1, 3, 4]. Combined with the observed fluence and the known distance to the source, this gives a typical event energy of $\sim 10^{51}$ ergs, comparable to the kinetic energy released in a supernova explosion. Such jets can be produced via the Blandford-Znajek effect [5] by a rapidly spinning black hole threaded by an ordered magnetic field [6–8], which is presumably generated inside the turbulent magnetized accretion disk, or by a millisecond magnetar [9–12]. The standard alternative mechanism is neutrino annihilation [13, 14], but it probably does not produce sufficient luminosity to explain most GRBs [15, 16].

In the present work we obtain global solutions of ultrarelativistic magnetically-dominated jets, confined by an external power-law pressure profile. We use time-dependent numerical magnetohydrodynamic (MHD) simulations in flat space-time (no gravity), and we focus on the relativistic *force-free* regime [5, 17–27], which corresponds to a magnetically-dominated plasma in which particle rest-mass and temperature are unimportant and are ignored. We work with spherical coordinates (r, θ, φ), but we also use cylindrical coordinates $R = r\sin\theta$, $z = r\cos\theta$. We set $c = r_0 = 1$, where c is the speed of light and r_0 is the radius of the compact object.

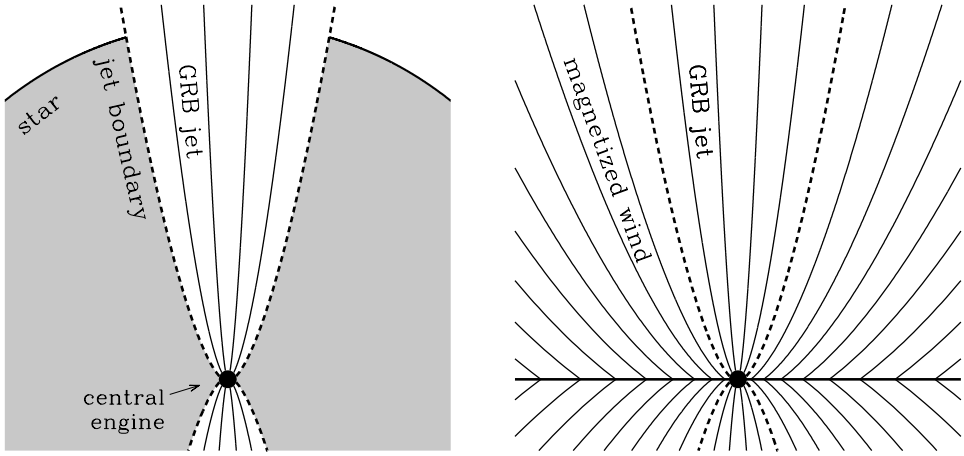

FIGURE 1. [Left panel, (a)] Cartoon of the large-scale structure of a GRB source (not to scale). The major elements are a central engine which launches a polar magnetically-dominated ultrarelativistic jet, and a gaseous stellar envelope (gray shading) which confines the jet. [Right panel, (b)] Idealized model studied in this paper. The star and the razor-thin disk are threaded by magnetic field lines (thin solid lines). Thick dashed lines indicate the field lines that separate the jet from the disk wind. The wind provides pressure support for the jet and plays the role of the gaseous stellar envelope as in the left panel.

MOTIVATION, PROBLEM SETUP, AND NUMERICAL METHOD

Figure 1a shows basic elements of a jet system: (i) a *central engine*, which could be a spinning black hole (BH) or neutron star, that produces (ii) a *highly magnetized jet* surrounded by a (iii) *confining medium*, e.g., the stellar envelope. Figure 1b shows our idealized approach to this problem. We replace the confining medium with a force-free disk wind tuned to have the same pressure profile as the confining medium. Magnetic field lines thread both the compact object and the razor-thin disk. We identify the field lines emerging from the compact object as the 'jet' and the lines from the disk as the 'wind.' In this idealized model, the force-free disk wind plays the role of the stellar envelope or gaseous disk wind that collimate the jet in a real GRB.

We perform the simulation in the domain $(r,\theta) \in (1,10^8) \times (0,\pi/2)$ and use the usual antisymmetry and outflow boundary conditions at $\theta = 0$ and $r = 10^8$ boundaries, respectively. We treat the central compact object as a perfect conductor with a uniform radial field on its surface, $B_r = 1$. We neglect all gravitational effects as they only slightly change the field shape even near the BH [28, 29]. The compact object and its field lines rotate at a fixed angular frequency $\Omega_0 = 0.25$ in our chosen units, which corresponds to a maximally spinning BH or a millisecond magnetar [30], and it is this magnetized rotation that launches and powers the jet. We choose a power-law profile for the vertical magnetic field at the surface of the razor-thin disk, $B_z(R) \propto R^{\nu-2}$, $0 < \nu < 2$, which leads to a power-law radial dependence of the wind confining pressure, $p \propto r^{2(\nu-2)}$ [30]. The simulations of hydrodynamic relativistic jets injected at an inlet within the presupernova core show complex interaction between the jet and the stellar envelope. We assume that the jet head has reached the surface of the progenitor star and a power-law pressure profile has been established within the jet (e.g., models JA-JC in [31]), and adopt that

pressure profile as the confining pressure profile. For our fiducial model we choose $\nu = 0.75$ which provides a good match to such a pressure profile and to the jet pressure profile found in GRMHD accretion simulations [28, 29]. We choose a Keplerian-like rotation profile in the razor-thin disk that smoothly connects to the rotation profile of the compact object.

We use a Godunov-type scheme [26] to numerically solve the time-dependent force-free equations of motion. Our code has been successfully used to model BH and neutron star magnetospheres [26, 28, 29, 32, 33]. To ensure accuracy and to properly resolve the jet, we use a numerical grid that approximately follows the magnetic field lines in the jet solution [33] and use a resolution of 2048x256. In order to speed up the computations, we evolve only the non-stationary region of the solution [30, 34]. Following this work we plan to use the same numerical scheme but optimized for the ultrarelativistic MHD regime [35–37] to systematically study the efficiency of matter acceleration.

SIMULATION RESULTS AND ANALYTICAL MODEL

Starting with a purely poloidal near-equilibrium initial magnetic field configuration for our fiducial model, we have run the force-free simulation until a time $t_{\rm f} = 10^7 r_0/c$. At the end of the calculation we obtained a time-steady solution out to a distance of $2\times10^6 r_0$. Fig. 2a shows the poloidal field of this steady state solution. The poloidal field in the final rotating state is nearly the same as in the initial non-rotating state, as in the case of the self-similar solutions discussed in Narayan et al. [33]. This is despite the fact that the final steady solution has a strong axisymmetric toroidal field $B_\varphi(r,\theta)$, which is generated by the rotating boundary conditions at the compact object and the disk. As a result of rotation, the solution develops a poloidal electric field $\vec{E}$ in the lab-frame, which is equal to $E = \Omega R B_p$, where Ω is the angular frequency at the foot-point of the local field line. This gives an outward Poynting flux $\vec{S} = \vec{E}\times\vec{B}/4\pi$ and associated angular power output per unit solid angle $dP/d\omega = r^2 S$. It also gives a drift speed $v = E/B$, and a corresponding Lorentz factor γ. The color-coding in the panels of Fig. 2a indicates the variation of γ with position in the steady solution. The Lorentz factor reaches up to a maximum ~ 1000 in this particular model. As Fig. 2a shows, the acceleration proceeds gradually and occurs over many decades in distance from the compact object.

Note that, at a given distance from the compact object, the maximum Lorentz factor is not achieved at either the jet-wind boundary or on the axis but at an intermediate radius inside the jet. For instance, at the slice $r = 5\times10^5$ shown in Fig. 3a, γ is maximum at $\theta_m \sim 0.006$, whereas the jet-wind boundary is located at $\theta_j \sim 0.16$. Thus, the jet consists of a slow inner spine, a fast edge, and a slow outer sheath which actually contains most of the power density, as Fig. 3b shows. Komissarov et al. [34] apparently observed this 'anomalous' effect in one of their solutions. Now we explain the origin of the effect.

Figure 2b shows the variation of the Lorentz factor with distance along two field lines emerging from the compact object. The field line that starts closer to the equator, with $\theta_{\rm fp} = 73^\circ$, rapidly accelerates once it is beyond $r \sim 10$. However, at $r \sim 10^3$ it switches to a different and slower mode of acceleration, reaching a final $\gamma \sim 500$ at $r = 2\times10^6$. In contrast, the field line that starts closer to the axis at $\theta_{\rm fp} = 21^\circ$ does not begin accelerating

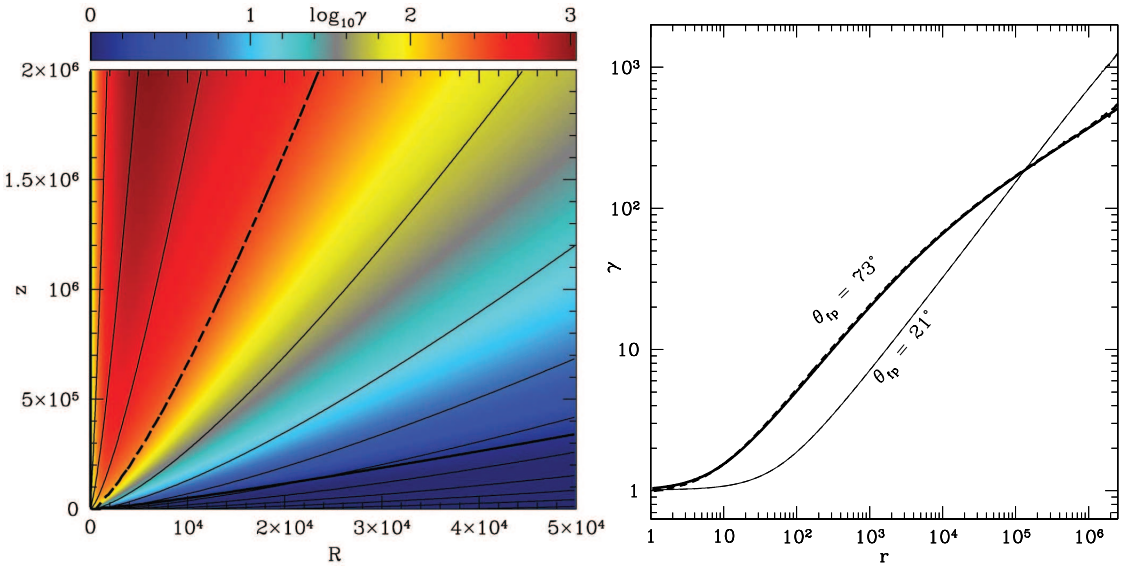

FIGURE 2. Results for the fiducial model with $\nu = 0.75$ which gives a confining pressure profile $p \propto r^{-2.5}$. [Left panel, (a)] Poloidal magnetic field lines (solid lines) overlaid on the color-coded (see bar at the top) Lorentz factor γ. The thick dashed line indicates the position of the field line that separates the jet from the disk wind (see Fig. 1a,b). The thick solid line is the Alfvén surface $\Omega R = 1$. Note that the maximum Lorentz factor is found inside the jet, and not at the jet-wind boundary (see Fig. 3a). [Right panel, (b)] Radial dependence of the Lorentz factor γ in the fiducial model for two field lines. One field line starts from the compact object at an angle $\theta_{\rm fp} \approx 73^\circ$ (thick lines), and the other starts at $\theta_{\rm fp} \approx 21^\circ$ (thin lines). Solid lines show the numerical solution and dashed lines show an analytical approximation [30] (the solid and dashed lines are virtually indistinguishable for $\theta_{\rm fp} = 21^\circ$). Note that the field line with $\theta_{\rm fp} = 73^\circ$ accelerates quickly as it moves away from the compact object but it then switches to a slower second regime of acceleration. In contrast, the field line with $\theta_{\rm fp} = 21^\circ$ begins accelerating only after it has moved a considerable distance from the compact object. However, it then maintains a rapid rate of acceleration without switching to the second acceleration regime. When the jet reaches the outer edge of the simulation at $r \sim 2 \times 10^6$, this field line has a very large bulk Lorentz factor $\gamma > 1000$, whereas the field line with $\theta_{\rm fp} = 73^\circ$ has a smaller $\gamma \sim 500$. Thus, the jet develops a fast core surrounded by a slower sheath.

until $r \sim 100$. It then accelerates rapidly almost until it reaches the outer radius, by which point it has a larger Lorentz factor ~ 1000 than the other field line. This inverted behavior causes the natural development of a fast structured spine and slow sheath that contains most of the power density. We have developed an analytical model to describe these two distinct acceleration regimes [30], and the resulting analytical prediction, shown with the dashed lines in Fig. 2b, agrees very well with the numerical simulation. We observe this kind of agreement for all field lines with $0 \leq \theta_{\rm fp} \leq 80^\circ$.

In addition to the fiducial model described above, we have simulated other models with ν in the range $0.5 \leq \nu \leq 1.25$. We find that all models with $\nu < 1$ are qualitatively similar, e.g., they all show the two acceleration regimes discussed above. Models with $\nu \geq 1$ are simpler since they display only the first acceleration regime. However, it is the models with $\nu < 1$ that are physically relevant because they satisfy the condition $\gamma\theta_j > 1$ required to explain the achromatic 'jet break' seen in GRB light curves [1, 30].

A very interesting question is what sets the terminal Lorentz factor of a relativistic

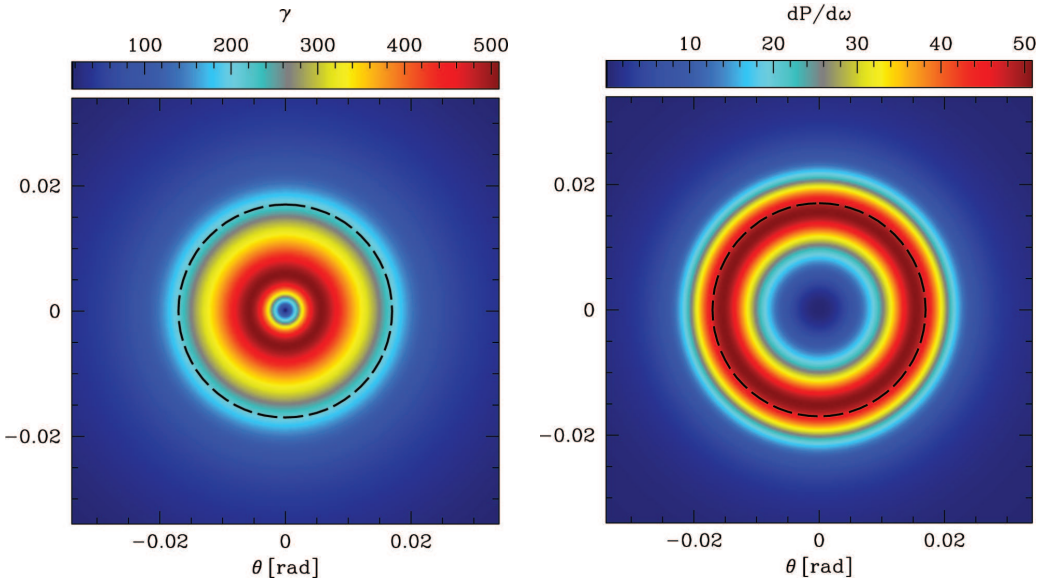

FIGURE 3. Face-on view of the lateral structure of the jet in the fiducial model at $r = 5 \times 10^5$ (2×10^{11} cm for a maximally spinning BH of mass $M = 3M_\odot$). The left panel (a) shows the color-coded (see bar on top) Lorentz factor, γ, and the right panel (b) shows the color-coded energy flux of the jet per unit solid angle, $dP/d\omega$. The dashed line shows the jet-wind boundary. Note that the maximum value of the energy flux, $dP/d\omega$, occurs at the jet-wind boundary, while γ is maximal inside the jet.

jet. In the context of the collapsar model the confining pressure on the jet is due to the stellar envelope, and therefore we expect the acceleration to continue only until the jet leaves the star. Once outside, the jet will probably become conical (monopolar). Such a field geometry is inefficient for accelerating particles for a wide range of jet initial magnetization as was shown in [38], i.e., the *Lorentz factor is determined by the size of the star* [30]. We note that once outside, current-driven instabilities may set in as the jet loses pressure support and much of the electromagnetic energy maybe converted into thermal energy [10, 39]. These additional topics are beyond the scope of the present paper and require simulations that model the loss of pressure to model the effect of progenitor star surface on the jet. By the time the jet breaks out of the star ($r \sim 10^5 - 10^6$), the physically relevant models with $0.6 \leq \nu \leq 1$ produce Lorentz factors $\gamma \sim 100 - 5000$ and opening angles $\theta_j \sim 10^{-3} - 0.2$ radians, perfectly consistent with observations of long GRBs. These are currently largest γ attained in a numerical magnetized jet simulation of long GRBs. We note that for low values of initial jet magnetization, its value may influence the jet Lorentz factor [34, 40].

We make a robust analytic prediction for the dependence of the maximum Lorentz factor on distance r along the jet, $\gamma_m(r) \approx (1/3 - 3)\sqrt{r}$. This applies to the whole physically relevant range of models $0.6 \leq \nu \leq 1$ [30]. For instance, for $r \sim 10^6$, the expected maximum Lorentz factor is $\gamma_m \sim \sqrt{r} \approx 10^3$, as confirmed in Fig. 2a,b. This formula can also be used to estimate the jet Lorentz factors not only of long GRBs but also AGN, short GRBs, and X-ray binary systems, where the jet is presumably confined by the wind from a radiatively inefficient accretion disk. The confining effect of the wind from such a disk with a characteristic radial extent $r \sim 50$ ceases around a distance

$\sim$ few $\times$ 100 along the jet [39]. Therefore, we would expect such a system to have a terminal Lorentz factor $\gamma \sim 1 - 10$, consistent with observations [41–44].

ACKNOWLEDGMENTS

We thank Vasily Beskin, Serguei Komissarov, Pawan Kumar, Matthew McQuinn, Shin Mineshige, Ehud Nakar, Tsvi Piran, and Dmitri Uzdensky for useful discussions. JCM has been supported by a Harvard Institute for Theory and Computation Fellowship and by NASA through Chandra Postdoctoral Fellowship PF7-80048 awarded by the Chandra X-Ray Observatory Center. The simulations described in this paper were run on the BlueGene/L system at the Harvard SEAS CyberInfrastructures Lab. This work was supported in part by NASA grant NNX08AH32G.

REFERENCES

1. T. Piran, *Reviews of Modern Physics* **76**, 1143–1210 (2005).
2. Y. Lithwick, and R. Sari, *ApJ* **555**, 540–545 (2001).
3. D. A. Frail, S. R. Kulkarni, R. Sari, S. G. Djorgovski, J. S. Bloom, T. J. Galama, D. E. Reichart, E. Berger, F. A. Harrison, P. A. Price, S. A. Yost, A. Diercks, R. W. Goodrich, and F. Chaffee, *ApJ* **562**, L55–L58 (2001).
4. A. Zeh, S. Klose, and D. A. Kann, *ApJ* **637**, 889–900 (2006).
5. R. D. Blandford, and R. L. Znajek, *MNRAS* **179**, 433–456 (1977).
6. R. Narayan, B. Paczynski, and T. Piran, *ApJ* **395**, L83–L86 (1992).
7. A. Levinson, and D. Eichler, *ApJ* **418**, 386 (1993).
8. P. Meszaros, and M. J. Rees, *ApJ* **482**, L29 (1997).
9. V. V. Usov, *Nature* **357**, 472–474 (1992).
10. M. Lyutikov, *New Journal of Physics* **8**, 119 (2006).
11. D. A. Uzdensky, and A. I. MacFadyen, *ApJ* **669**, 546–560 (2007).
12. N. Bucciantini, E. Quataert, J. Arons, B. D. Metzger, and T. A. Thompson, *MNRAS* **380**, 1541 (2007).
13. S. E. Woosley, *ApJ* **405**, 273–277 (1993).
14. A. I. MacFadyen, and S. E. Woosley, *ApJ* **524**, 262–289 (1999).
15. R. Popham, S. E. Woosley, and C. Fryer, *ApJ* **518**, 356–374 (1999).
16. T. Di Matteo, R. Perna, and R. Narayan, *ApJ* **579**, 706–715 (2002).
17. P. Goldreich, and W. H. Julian, *ApJ* **157**, 869 (1969).
18. I. Okamoto, *MNRAS* **166**, 683–702 (1974).
19. R. D. Blandford, *MNRAS* **176**, 465–481 (1976).
20. R. V. E. Lovelace, *Nature* **262**, 649–652 (1976).
21. D. MacDonald, and K. S. Thorne, *MNRAS* **198**, 345–382 (1982).
22. R. V. E. Lovelace, and M. M. Romanova, *ApJ* **596**, L159–L162 (2003).
23. C. Fendt, M. Camenzind, and S. Appl, *A&A* **300**, 791 (1995).
24. S. S. Komissarov, *MNRAS* **326**, L41–L44 (2001).
25. S. S. Komissarov, *MNRAS* **336**, 759–766 (2002).
26. J. C. McKinney, *MNRAS* **367**, 1797–1807 (2006).
27. R. V. E. Lovelace, L. Turner, and M. M. Romanova, *ApJ* **652**, 1494–1498 (2006).
28. J. C. McKinney, and R. Narayan, *MNRAS* **375**, 513–530 (2007).
29. J. C. McKinney, and R. Narayan, *MNRAS* **375**, 531–547 (2007).
30. A. Tchekhovskoy, J. C. McKinney, and R. Narayan, *MNRAS, doi: 10.1111/j.1365-2966.2008.13425.x (arXiv:0803.3807)* (2008).
31. W. Zhang, S. E. Woosley, and A. I. MacFadyen, *ApJ* **586**, 356–371 (2003).
32. J. C. McKinney, *MNRAS* **368**, L30–L34 (2006).
33. R. Narayan, J. C. McKinney, and A. J. Farmer, *MNRAS* **375**, 548–566 (2007).

34. S. S. Komissarov, M. V. Barkov, N. Vlahakis, and A. Königl, *MNRAS* **380**, 51–70 (2007).
35. C. F. Gammie, J. C. McKinney, and G. Tóth, *ApJ* **589**, 444–457 (2003).
36. A. Mignone, and J. C. McKinney, *MNRAS* **378**, 1118–1130 (2007).
37. A. Tchekhovskoy, J. C. McKinney, and R. Narayan, *MNRAS* **379**, 469–497 (2007).
38. V. S. Beskin, I. V. Kuznetsova, and R. R. Rafikov, *MNRAS* **299**, 341–348 (1998).
39. J. C. McKinney, *MNRAS* **368**, 1561–1582 (2006).
40. M. V. Barkov, and S. S. Komissarov, *preprint (arXiv:0801.4861)* (2008).
41. S. G. Jorstad, A. P. Marscher, M. L. Lister, A. M. Stirling, T. V. Cawthorne, W. K. Gear, J. L. Gómez, J. A. Stevens, P. S. Smith, J. R. Forster, and E. I. Robson, *AJ* **130**, 1418–1465 (2005).
42. R. P. Fender, T. M. Belloni, and E. Gallo, *MNRAS* **355**, 1105–1118 (2004).
43. R. Fender, K. Wu, H. Johnston, T. Tzioumis, P. Jonker, R. Spencer, and M. van der Klis, *Nature* **427**, 222–224 (2004).
44. E. Nakar, *Phys. Rep.* **442**, 166–236 (2007).